# Macroscopic description of fast heavy-ion-induced desorption yields

E. Nieschler, B. Nees, and H. Voit

*Physikalisches Institut der Universität Erlangen-Nürnberg, D-8520 Erlangen, West Germany*

P. Beining and J. Scheer

*Fachbereich 1 (Physik/Elektrotechnik), Universität Bremen, D-2800 Bremen, West Germany*

(Received 13 October 1987)

The dependence of fast heavy-ion-induced desorption yields on the primary-ion energy has been measured for a number of different target materials as well as for different primary ions. The primary-ion energies cover a relatively large range with corresponding energy losses between 2.6 and 64 MeV cm² mg⁻¹. The observed energy dependences can be understood in the framework of a simple macroscopic model.

## I. INTRODUCTION

It is well known since the investigations of Macfarlane and co-workers (see Ref. 1) that MeV-energy heavy ions can be used to desorb fragile and otherwise involatile organic molecular ions from dielectric sample surfaces. Besides the applied aspect of the heavy-ion-induced desorption (HIID), the desorption mechanism itself is of great interest. In order to elucidate this mechanism a number of experiments have been carried out by several authors.[2] For these experiments mainly heavy-ion beams from particle accelerators have been used since the primary-ion parameters can be chosen in a controlled way. The present paper reports such an investigation performed to study the dependence of the desorption yield on the energy of MeV-energy primary ions from particle accelerators. The paper is an extension of previously published studies.[3,4] The experimental data are described in terms of a macroscopic model of the desorption process. The model is akin to the thermal model for particle induced desorption of Lucchese.[5] Other models developed to describe HIID can be found in Refs. 6–9.

## II. EXPERIMENTAL PROCEDURE

The experiments have been carried out with oxygen (9–42 MeV) and sulfur (12–60 MeV) beams of the Erlangen EN tandem accelerator and neon (25–260 MeV) and krypton (30–320 MeV) beams of the accelerator VICKSI of the Hahn-Meitner-Institute, Berlin. The experimental setup used is essentially the same as that described in Ref. 3 with the additional modifications of Ref. 4. The energy dependence was measured without changing the energy of the heavy-ion beam by means of a method described in Ref. 10. This method has the advantage that the beam spot on the sample is always identical for all measured energies.

The primary ions impinging on the sample surface exhibit an equilibrium-charge-state distribution since the accelerator beam is scattered from a thick tantalum disc to produce a broad energy spectrum for the primary ions. Besides this, tantalum recoil ions arise and hit the sam-

ple. In order to exclude all secondary ions desorbed by the recoil ions from the analysis, the following provisions have been made: (i) In case of the low-energy experiments ($^{16}$O and $^{32}$S beams), where the recoil energy is relatively small, all secondary ions desorbed by primary ions with an energy below the maximum recoil energy have been rejected, (ii) in case of the $^{86}$Kr beam a time-of-flight identification of the recoils has been performed and used to eliminate recoil-induced desorption events, and (iii) in case of the $^{22}$Ne beam a 5-$\mu$m Ni foil was used to prevent the recoils from hitting the sample.

It should be noted that all yields reported in this paper are relative yields (see Ref. 11). This is due to the unknown efficiency of the mass spectrometer, which is constant during one particular experimental run but may vary slightly from run to run due to different modes of operation of the channel plates. It was found that these effects result in relative yields which vary by 20% at the most for different runs.

If two molecular ions are desorbed simultaneously by one primary ion and if a time-to-amplitude converter is used as electronic clock (as in the present case) which accepts only one stop signal after the start signal, the desorption yield for the heavier mass is suppressed compared to that of the lighter mass. The effect ("schatten" effect) can be ignored for light primary ions with relatively small energy losses since the desorption multiplicity is approximately one; it plays, however, a role for the desorption yield induced by heavier projectiles. In order to keep this effect small only limited sections of the total mass spectra containing the mass peaks of interest were analyzed. It should be noted that the multiplicity does not change with primary-ion energy in the case of the two heaviest projectiles (S, Kr) since the energy loss remains almost constant in the energy range studied. Thus, the measured energy dependences are not influenced by the schatten effect.

The samples which were used for the measurements are the $\alpha$-amino acids (*DL*-type) valine ($m = 117$ amu), threonine ($m = 119$ amu), glutamine ($m = 146$ amu), and glutamic acid ($m = 147$ amu). Besides this we investigated cesium iodide (CsI) and the saltlike compounds tetra-
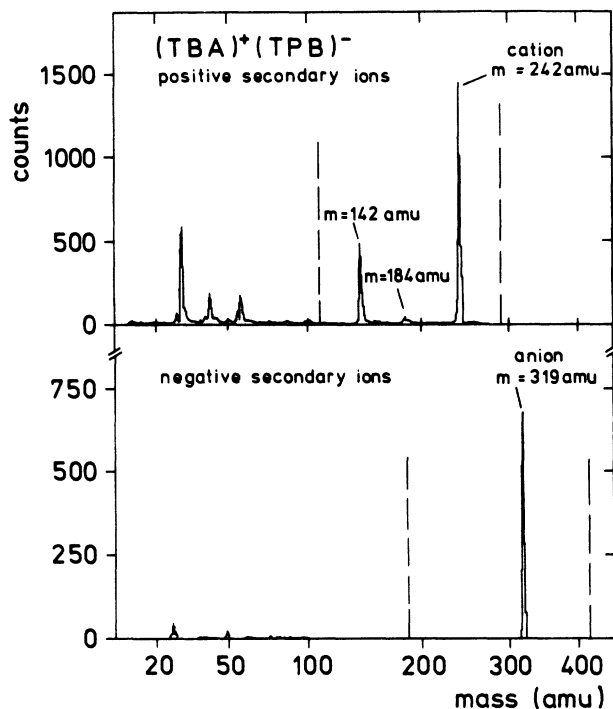
FIG. 1. Mass spectra for positive (upper part) and negative (lower part) molecular ions desorbed by primary ions from a $(TBA)^+(TPB)^-$ sample. The vertical dashed lines indicate the mass ranges for which the actual measurements have been performed.



FIG. 2. Dependence of the $[M+H]^+$ yields for different amino acids on the energy of the primary ion. The primary ion is $^{16}O$. $M$ indicates the molecular mass. Energy losses $dE/dx$ for $^{16}O$ primary ions are indicated in the upper part of the figure.

butyl ammonium tetraphenylborate [in the following the cation with $m = 242$ amu and the anion with $m = 319$ amu are abbreviated $(TBA)^+$ and $(TPB)^-$, respectively] and 2,3-diphenyl-3-triphenylphosphoranyliden-1-(triphenyl-phosphonium)-bromide (Ref. 12) [abbreviated as $(TPP)^+Br^-$; the mass of the cation $(TPP)^+$ is $m = 715$ amu]. With the exception of CsI all samples investigated are organic compounds. Figure 1 shows, as an example, typical mass spectra for the $(TBA)^+(TPB)^-$ sample. In the actual experiment only a small section of the total spectrum (indicated by the dashed vertical lines) was analyzed (see above).

The samples were deposited on a thin aluminized Mylar foil (290 $\mu g\,cm^{-2}$ Mylar, 20 $\mu g\,cm^{-2}$ Al) by means of the electrospray method.[13] Sample thicknesses were of the order of 15–40 $\mu g\,cm^{-2}$. The CsI sample was prepared by vacuum evaporation.

## III. EXPERIMENTAL RESULTS

### A. Polar samples

Figures 2 and 3 show the energy dependence of the desorption yield $Y$ for the molecular ions $[M+H]^+$ and $[M-H]^-$ desorbed from amino acid samples by $^{16}O$ primary ions ($M$ indicates the molecular mass). The energy loss of the $^{16}O$ projectiles is given in the upper part of the figures. It was calculated according to the Bragg additivity rule from the energy-loss data of Refs. 14 and 15
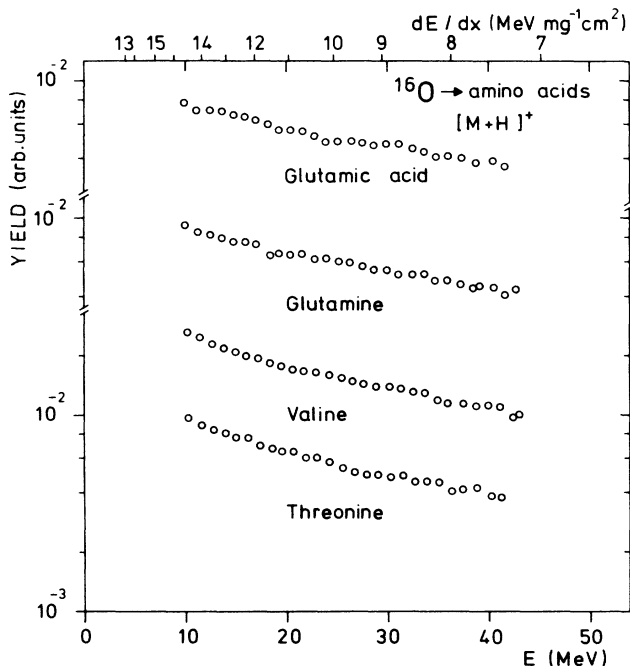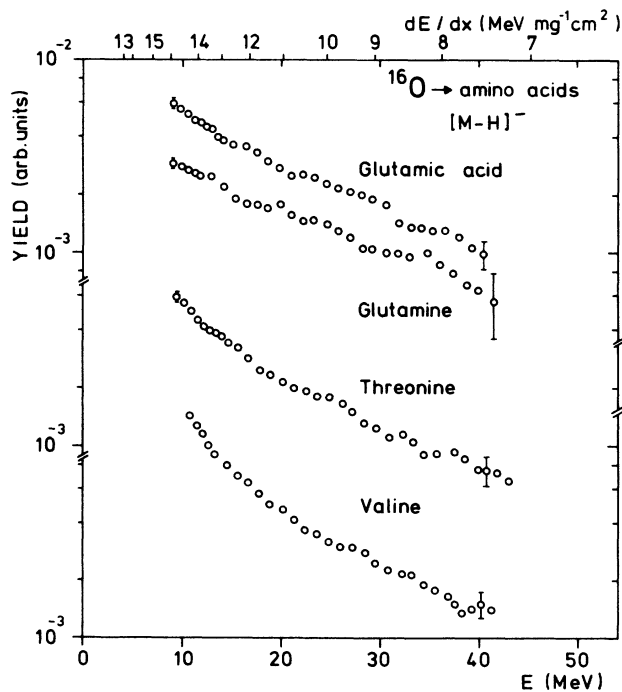


FIG. 3. Yield functions for $[M-H]^-$ secondary ions desorbed by $^{16}O$ primary ions.
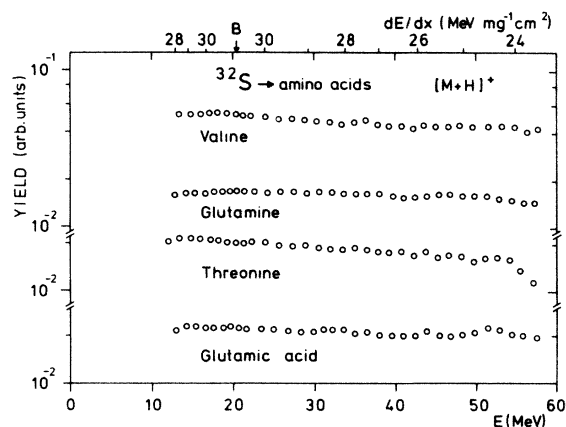
FIG. 4. $^{32}$S-induced yield functions for $[M+H]^+$ secondary ions desorbed from different amino acid samples. $B$ indicates the approximate position of the energy-loss maximum (Bragg maximum).



FIG. 6. $^{22}$Ne-induced yield functions for $[M-COOH]^+$ (solid circles) and $[M+H]^+$ (open circles) secondary ions desorbed from a valine sample. The solid lines are model calculations (see Sec. IV) performed with the $(R_F, R_C)$—values as given in the figure.

(the same holds for all other primary ions and compounds investigated in this work).

The $[M+H]^+$ yields exhibit the same energy dependence for all amino acids investigated (see Fig. 2). The $[M-H]^-$ yields decrease much faster with increasing primary-ion energy than the $[M+H]^+$ yields (see Fig. 3); the energy dependences are approximately the same for all $[M-H]^-$ ions. This result agrees with the experimental data reported already in Refs. 3 and 4.

Figures 4 and 5 show the $^{32}$S-induced desorption yields for the amino acids. The observed energy dependences are less pronounced than for the $^{16}$O-induced data. This is related to the fact that the energy deposited by the $^{32}$S ions changes less in the energy range investigated than in the $^{16}$O case (see the $dE/dx$ axis of Figs. 4 and 5). Again the $[M-H]^-$ yields decrease faster with energy than the $[M+H]^+$ yields. All $[M+H]^+$ yields exhibit approximately the same energy dependence; the same holds for the $[M-H]^-$ yields even though small differences are observed.
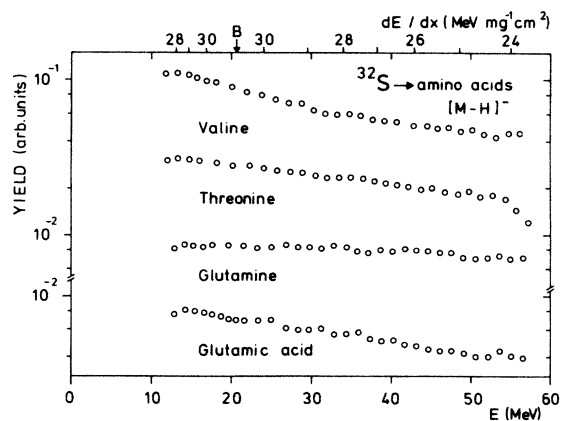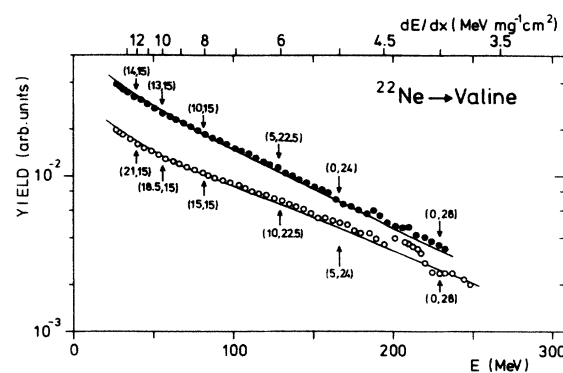
$^{22}$Ne-induced yields for positive molecular ions desorbed from a valine sample are shown in Fig. 6. They exhibit a pronounced energy dependence due to the large energy loss difference of the $^{22}$Ne ions (see the $dE/dx$ axis of Fig. 6). The $^{86}$Kr-induced data of Fig. 7 show similar energy dependences as the $^{32}$S-induced data. In both cases the energy ratios determined for the smallest and highest primary-ion energies are approximately the same within the energy range studied.

The $[M+H]^+$ yields desorbed by different primary ions from valine are shown as a function of the primary-ion energy loss $dE/dx$ in Fig. 8. The relative yields obtained for $^{12}$C, $^{16}$O and $^{32}$S ions are normalized to each other. This could be easily done since $^{16}$O induced valine yields were measured simultaneously with the same experimental setup used for the $^{12}$C and $^{32}$S irradiations. The $^{22}$Ne and $^{86}$Kr data represent the plain experimental-



FIG. 5. $^{32}$S-induced yield functions for $[M-H]^-$ ions desorbed from amino acid samples.
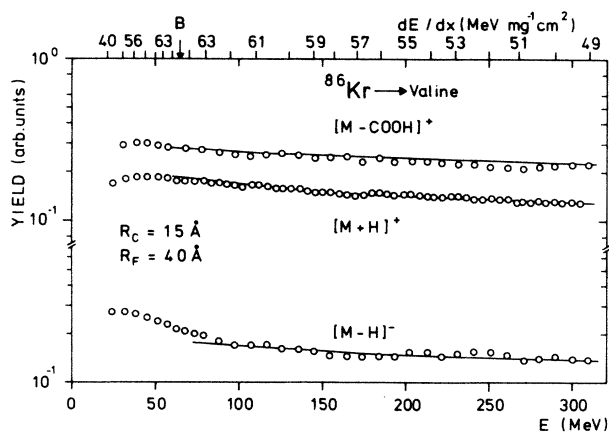


FIG. 7. $^{86}$Kr-induced yield functions for positive and negative secondary ions desorbed from a valine sample. $B$ indicates the approximate position of the energy-loss maximum of $^{86}$Kr in valine. For the solid lines, see Sec. IV.
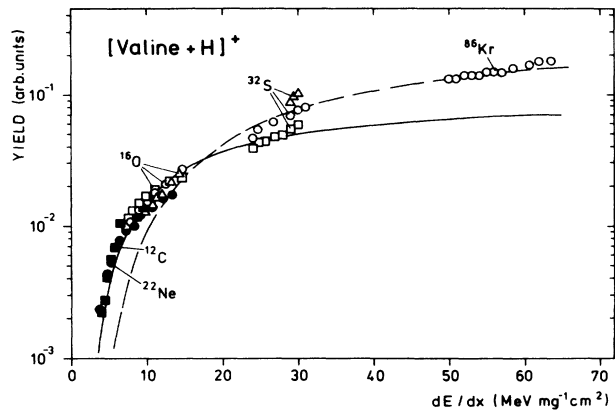
NIESCHLER, NEES, VOIT, BEINING, AND SCHEER

FIG. 8. Secondary-ion yield for $[M + H]^+$ molecular ions desorbed from a valine sample by different primary ions as a function of the energy deposited by the primary ions. O and ● refer to data obtained in this work. Data points indicated by □ and ■ and △ are from Refs. 3 and 11, respectively. The solid and dashed line are predictions of the macroscopic model with $R_C = R_F = 15$ Å and $R_C = 15$ Å, $R_F = 40$ Å, respectively. For details see text.
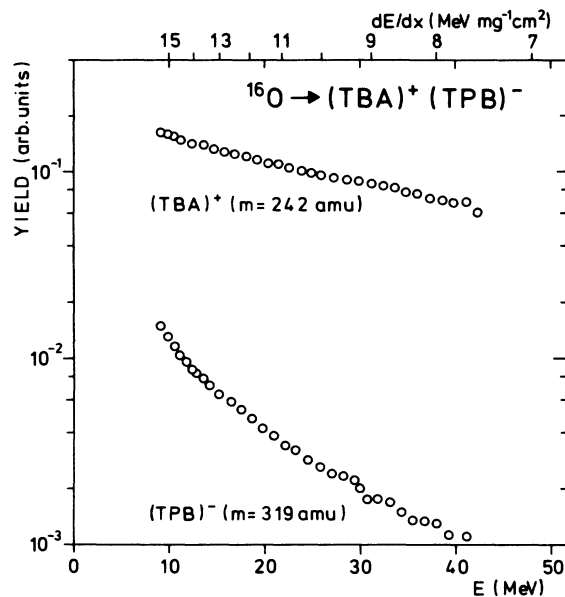


FIG. 10. $^{16}$O-induced yield functions for the cation and the anion of a $(TBA)^+(TPB)^-$ sample.

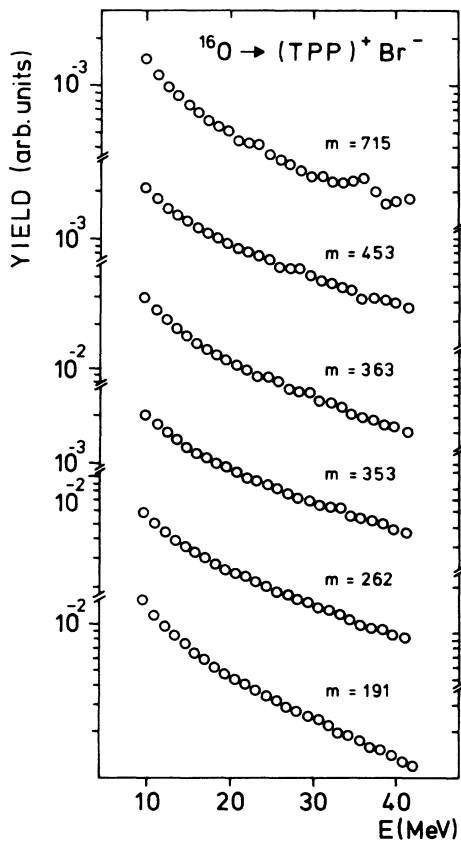ly determined relative yields which have to be shifted eventually by up to 20% (see Sec. II).

## B. Ionic samples

Figure 9 shows the $^{16}$O-induced data for the $(TPP)^+Br^-$ sample. Yield functions are measured for the molecular cation and several fragment ions. The fragment mass with $m = 191$ amu corresponds to the di-
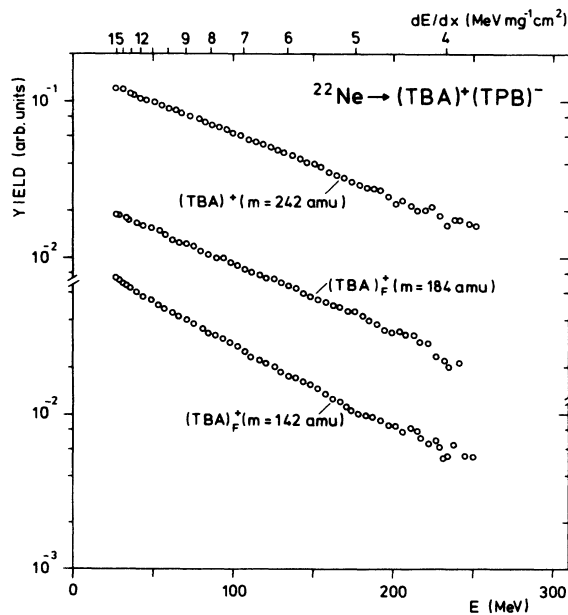


FIG. 9. $^{16}$O-induced yield functions for positive secondary ions desorbed from a $(TPP)^+Br^-$ sample. The molecular cation has the mass $m = 715$ amu.



FIG. 11. $^{22}$Ne-induced yield functions for the cation $(TBA)^+$ and two fragment ions $(TBA)_F^+$ desorbed from the $(TBA)^+(TPB)^-$ sample.

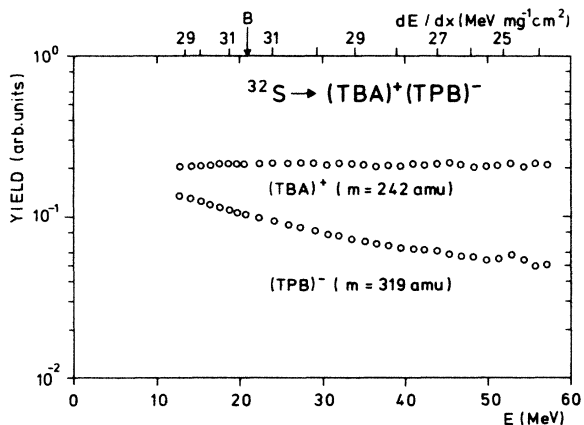FIG. 12. $^{32}$S-induced yield functions for the cation and the anion of the compound (TBA)$^+$(TPB)$^-$. $B$ indicates the approximate position of the energy-loss maximum.

phenylcyclopropenylium cation. The slopes of the yield functions for the different masses are almost identical. They agree with those observed for the negative molecular ions desorbed by $^{16}$O ions from amino acid samples. Only the $m = 191$ yield function exhibits a somewhat steeper slope.

Figures 10–13 show yield functions obtained for $^{16}$O, $^{22}$Ne, $^{32}$S, and $^{86}$Kr primary ions and a (TBA)$^+$(TPB)$^-$ sample. Data were taken for the molecular ions (TPB)$^-$ and (TBA)$^+$ as well as for the fragment ions (TBA)$_F^+$ with masses $m = 142$ and 184 amu. The (TBA)$^+$ and (TPB)$^-$ yield functions obtained for $^{16}$O primary ions exhibit ap-

proximately the same slopes as the $[M + H]^+$ and $[M - H]^-$ yield functions obtained with $^{16}$O primary ions for the amino acids. The $^{22}$Ne data (see Fig. 11) decrease exponentially with increasing energy and exhibit slopes which increase with decreasing mass of the desorbed secondary ion. The $^{32}$S-induced (TBA)$^+$ yield (see Fig. 12) is constant within the energy range studied (the energy loss changes by 30%). It is interesting to note that the $^{86}$Kr-induced (TBA)$^+$ and (TBA)$_F^+$ ($m = 184$ amu) yield functions exhibit a positive slope, i.e., the yield increases with decreasing energy loss (30% change within the energy range studied).

Figures 14–16 show $^{16}$O-, $^{22}$Ne-, and $^{32}$S-induced desorption yields for the sample CsI. Yields have been measured for the cation and the anion as well as for the (CsI)Cs$^+$ and (CsI)I$^-$ cluster ions. It is interesting to note that the I$^-$ yield is noticeable smaller than the Cs$^+$ yield in all cases measured. The $^{16}$O-induced Cs$^+$ and I$^-$ yield functions (see Fig. 14) represent the only case where a steeper slope was observed for the positive secondary ion than for the negative secondary ion. The $^{32}$S-induced yields are almost constant within the measured energy
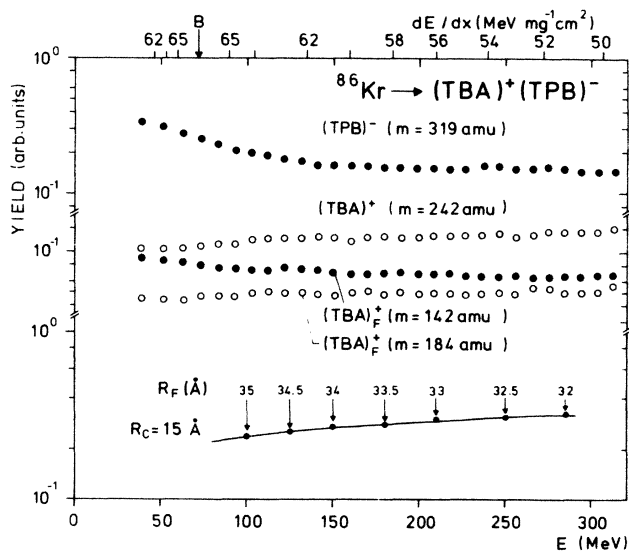


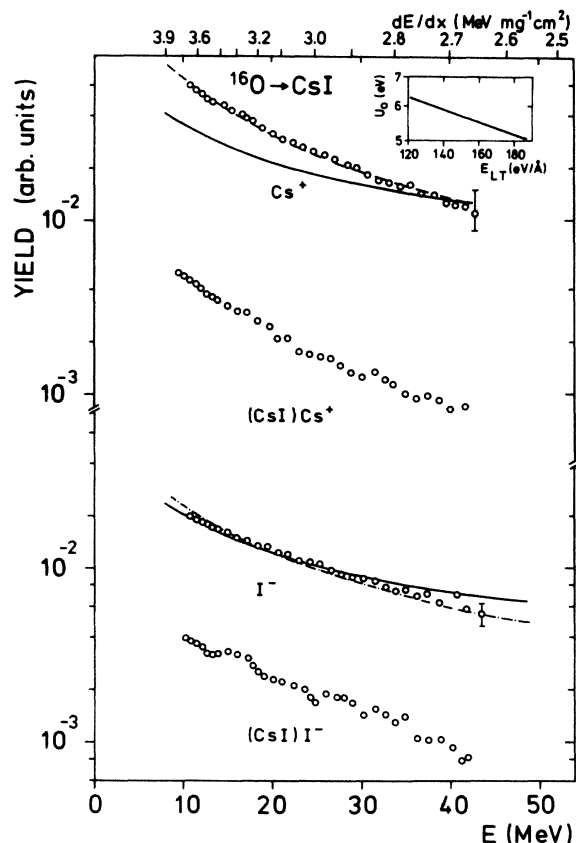FIG. 13. $^{86}$Kr-induced yield functions for (TBA)$^+$(TPB)$^-$. In the lower part of the figure a model calculation (see Sec. IV) is shown for which energy-dependent values of the fragmentation radius $R_F$ were used (the $R_F$ values are indicated along the solid line). The calculations are performed with the core radius $R_C = 15$ Å and the valine parameters of Table I.



FIG. 14. $^{16}$O-induced yield functions for a CsI sample. The solid lines are the predictions of the macroscopic model ($R_C = 20$ Å, $R_F = 0$). The dashed line is obtained if the effective surface binding energy is decreased with increasing energy loss (according to the inset) in order to simulate the effect of the Coulomb repulsion. The dashed-dotted line is obtained for $R_C = R_F = 20$ Å. To obtain the $E_{LT}$ values multiply the $dE/dx$ values by 45.1.
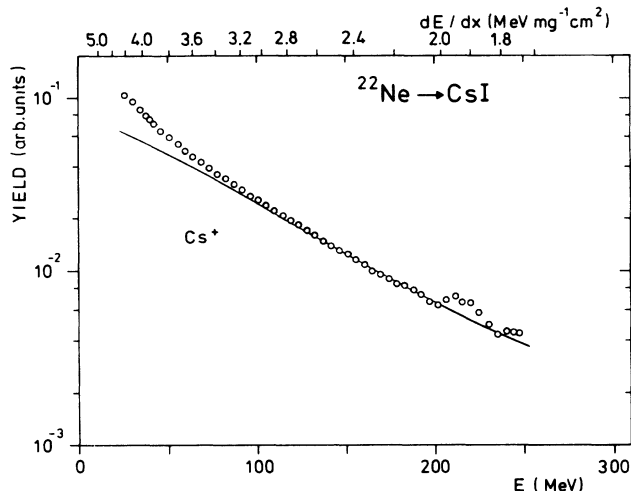
FIG. 15. $^{22}$Ne-induced yield functions for Cs$^+$ ions desorbed from a CsI sample. The solid line is the prediction of the macroscopic model. It was obtained with $R_F = 0$ Å and $R_C$—values which were smoothly increased from 15 Å to 20 Å between the lowest and highest primary-ion energies.

range (see Fig. 16). It should be noted, however, that the energy loss stays also almost constant.

In summary, the experimental results exhibit the following features.

(i) The energy dependences of the secondary-ion yield for ions desorbed from the same sample by different primary ions reflect roughly the changing energy loss of the primary ions without exhibiting a proportionality between yield and energy loss (see Fig. 8).

(ii) Yield functions for different samples desorbed by the same primary ion show a dependence on the chemical composition.

(iii) The energy dependences of negative ion yields differ from those for positive secondary ions; normally the energy dependence is more pronounced for negative ions.
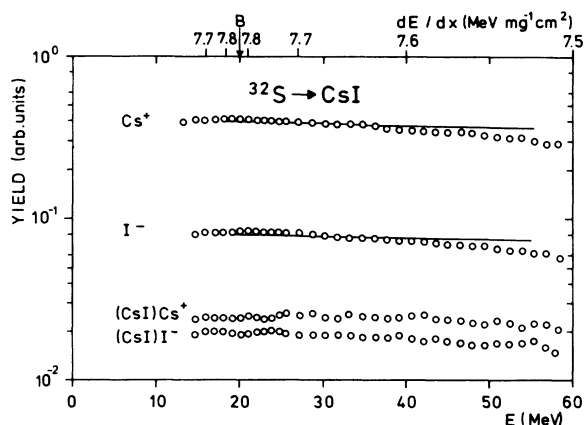


FIG. 16. $^{32}$S-induced yield functions for positive and negative secondary ions desorbed from a CsI sample. $B$ indicates the approximate position of the energy-loss maximum. The solid lines are predictions of the macroscopic model ($R_C = 20$ Å, $R_F = 0$).

Point (i) is illustrated in Fig. 8 for $[M+H]^+$ ions desorbed from a valine sample by different primary ions. From this figure a threshold for the energy loss of roughly 2.9 MeV cm$^2$ mg$^{-1}$ can be deduced. This energy loss is at least necessary in order to initiate the desorption of a $[M+H]^+$ molecular ion from a valine sample. The result is in agreement with the observation made by Dück[16] that MeV-energy $\alpha$ particles with a maximum energy loss of 2.3 MeV cm$^2$ mg$^{-1}$ are not able to desorb molecular ions from a valine sample.

Two remarkable deviations from the above general behavior exist, however: (i) the $^{86}$Kr-induced yield functions for the (TBA)$^+$(TPB)$^-$ sample ($m = 184$ and 242 amu) increase with decreasing energy loss and (ii) the $^{16}$O-induced Cs$^+$ yield depends more strongly on the primary-ion energy than the $^{16}$O-induced I$^-$ yield.

## IV. MACROSCOPIC DESCRIPTION OF THE YIELD FUNCTIONS

An attempt was made to understand the measured yield functions—at least qualitatively—from a macroscopic point of view. For this purpose it is assumed that molecular ions are only desorbed from the very surface of the sample and that the desorption probability $P$ can be expressed by

$$P \propto e^{-U_0/E_s} , \tag{1}$$

where $U_0$ denotes an effective binding energy of the molecule bound to the sample surface and $E_s$ that portion of the energy deposited by the primary ion along the ion path which reaches the sample surface at the molecular site. For Eq. (1) to be valid one has to assume that at least a local thermal equilibrium exists. This assumption is approximately fulfilled as can be seen from a comparison of the time scales involved in the desorption of the molecule [the time needed by a surface molecule with $E_{kin} \approx 1$ eV (see Ref. 11) to leave the region of the binding force is of the order of $10^{-13}$ s] and the dissipation of the primary ion energy (see below).

The energy $E_s$ in Eq. (1) originates from all points $P_k$ along the primary-ion trajectory having a distance between zero and $X^{max}$ from the sample surface (see Fig. 17). Since the time needed by the primary ion to traverse the distance $X^{max}$ (typically 100 Å, see below) is rather short ($10^{-15}$–$10^{-16}$ s) it can be assumed that the energy dissipation starts simultaneously at all points $P_k$ ($t_j = 0$). At the time $t_j > 0$ the contribution from the point $P_k$ to the energy available at the surface point $A_i$ with the distance $r_i^k$ from $P_k$ is $E_s(r_i^k, t_j)$. Point $A_i$ has the distance $R_i$ from the primary-ion trajectory. With these geometrical considerations and the assumptions made above the relative secondary-ion yield $Y$ can be expressed as

$$Y \propto \sum_{i,j,k} R_i \Delta R \exp[-U_0/E_s(r_i^k, t_j)] . \tag{2}$$

Equation (2) represents a threefold sum over all time intervals, all points $P_k$ along the primary-ion trajectory, and all weighted annular areas with radii $R_i$ (the weighting factor is the desorption probability $P$) and constant
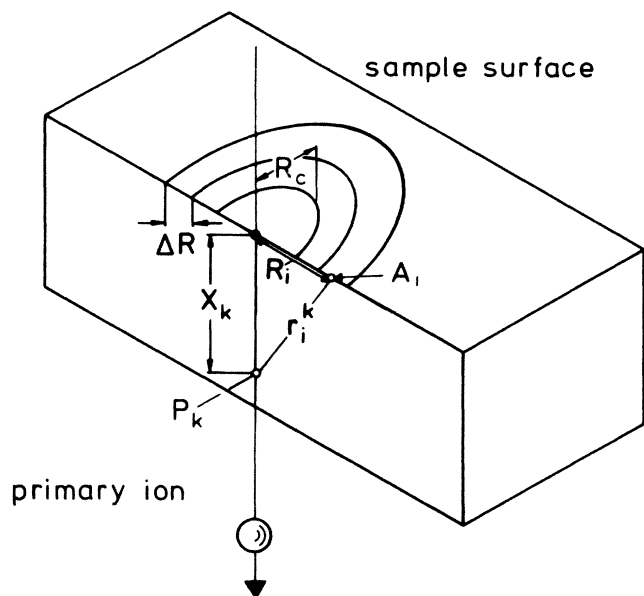
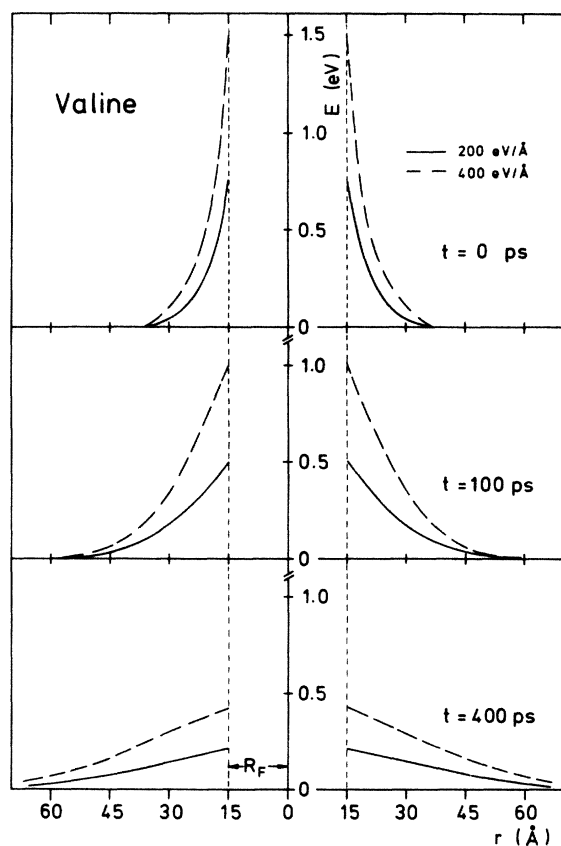FIG. 17. Geometrical aspects of the macroscopic picture used to describe the measured yield functions.

energy density. It should be noted that in case of fragile molecules a circular area around the primary-ion trajectory with radius $R_F$ was not taken into account for the calculation of the yield $Y$. The reason is that one has to assume that fragile molecules will be totally fragmented within this area due to the high-energy density.

To calculate the temporal and spatial distribution of the energy deposited at $P_k$ by the primary ion we have used an expression given by Mozumder[17]

$$E(r,t)=kT_0(1+4\delta t/R_C^2)^{-1}\exp[-r^2/(R_C^2+4\delta t)]\qquad(3)$$

with $k$ the Boltzmann factor and $\delta$ the thermal diffusivity given by $\delta=\kappa/\rho c_v$, where $\kappa$, $c_v$, and $\rho$ are the thermal conductivity, the specific heat at constant volume, and the density of the sample, respectively. The quantity $T_0$ is the effective temperature of the hot core and is given in terms of the linear energy transfer $E_{LT}$ as

$$T_0=E_{LT}(\pi\rho c_v R_C^2)^{-1}\ .\qquad(4)$$

The hot core represents a cylindrical region around the primary-ion trajectory in which the overwhelming fraction of the energy deposited is concentrated. The radius of the hot core $R_C$ (hot core radius) can be equated according to Ref. 17 with the maximum impact parameter $b_{max}$ used in the Bohr theory for the electronic stopping power[18] ($b_{max}$ is related to the minimum energy a free



FIG. 18. Spatial energy distribution for valine calculated according to Eq. (3) for different values of the linear energy transfer ($E_{LT}=200$ and 400 eV/Å, respectively) and different times $t$. $R_C=15$ Å was used. The vertical dashed lines indicate the hot core region.
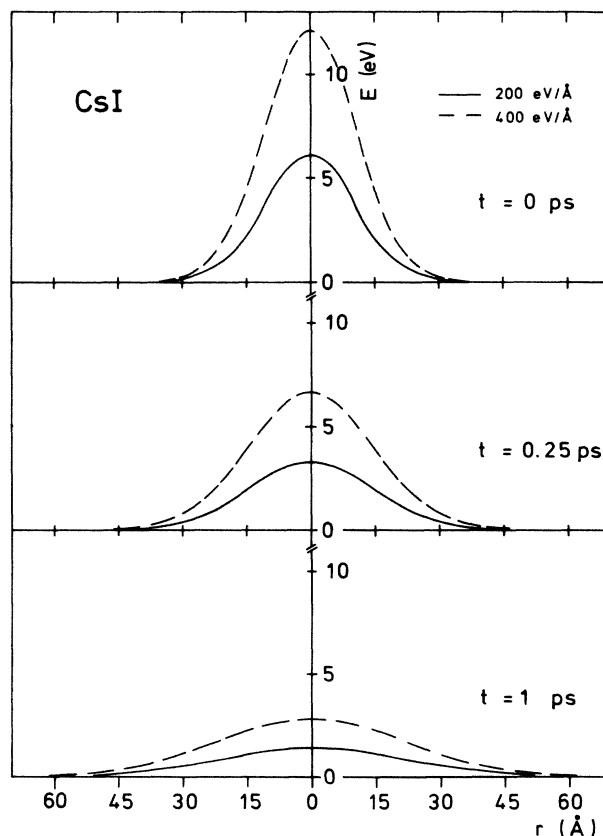


FIG. 19. Spatial energy distribution for CsI calculated with Eq. (3). For details see the caption of Fig. 18.

TABLE I. Properties of the samples valine and CsI used for the model calculations.

| Compound | $\rho$ (kg m$^{-3}$) | $c_p$ (J kg$^{-1}$K$^{-1}$) | Reference | $\kappa$ (J m$^{-1}$s$^{-1}$) | Reference | $U_0$ (eV) | Reference |
|---|---|---|---|---|---|---|---|
| Valine | $1.32 \times 10^3$ | $1.45 \times 10^3$ (25 °C) | 20 | 0.02 (30 °C) | 21 | 1.69 | 19 |
| CsI | $4.5 \times 10^3$ | $0.2 \times 10^3$ (25 °C) | 22 | 1.2 (0 °C) | 21 | 6.21 | 22 |

electron can receive from the primary ion in a minimum momentum transfer). Since $b_{max}$ is proportional to the primary-ion velocity the same proportionality is expected for $R_C$ according to Ref. 17. For small primary-ion velocities (smaller or comparable to the orbital velocities of the electrons) a minimum core radius exists which is estimated in Ref. 17 to be approximately $R_C(min) \approx 15$ Å (corresponding to the range of 100-eV electrons in water).

Figures 18–21 show the spatial and temporal energy distributions calculated for valine and CsI samples according to Eq. (3) with $R_C = 15$ Å. The quantities $\kappa$, $\rho$, and $c_v$ used for these calculations are given in Table I. It should be noted that we had to use $c_p$ values (specific heat at constant pressure) instead of $c_v$ values, since $c_v$ values could not be found in the literature. This is, however, justified since it is known (see Ref. 23) that $c_v$ values are typically only 5% smaller than $c_p$ values. The $c_p$ value listed for valine was measured for L-valine;[20] we assume, however, that $c_p$ values for L- and DL-valine (the latter was investigated in this work) are not significantly different. The heat conductivity of valine has not been measured up to now. Therefore we used the $\kappa$ value for cellulose. It is known that this value is comparable with the heat conductivity of a number of organic compounds similar to valine (see Ref. 21). The $c_v$ and $\kappa$ values were

assumed to be temperature independent to simplify the calculations. This is justified since these values do not change very much in the temperature range between room temperature and melting point temperature;[20,24] besides this, changes of the order of 50% in the thermal diffusivity do not have a serious impact on the absolute values of $Y(E)$ as will be shown below. The effective binding energies $U_0$ needed for the calculation of the relative yields are also given in Table I. The $U_0$ value for valine was deduced from the measured sublimation heat,[19] for CsI the energy was used which is necessary to remove an ion from the sample.[22]

The influence of the different parameters on the results of yield calculations performed with Eq. (2) was studied. Figure 22 shows the results for the $^{16}$O-induced desorption from a valine sample. We have changed in each case only one parameter (indicated in the figure) and used otherwise as standard parameter set the values of Table I together with $R_C = R_F = 15$ Å and $X^{max} = 50$ Å. It is obvious from Fig. 22 that the effective surface-binding energy has a rather strong influence on the slope of the yield function whereas the thermal diffusivity is less sensitive to the outcome of the calculations. It is interesting to note that energies deposited at $X_k > 50$ Å do not contribute much to the energy available at the sample surface. Similar results are obtained for the investigations of the $^{16}$O-induced desorption from a CsI sample (see Fig. 23). The standard parameter set consists of the parameters
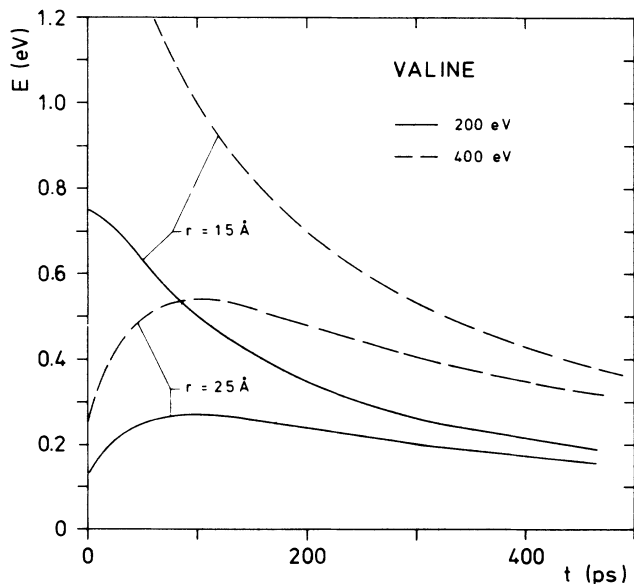


FIG. 20. Temporal energy distributions for valine calculated according to Eq. (3) for two different distances from the ion track and two different values for the linear energy transfer $E_{LT}$. $R_C = 15$ Å was used.
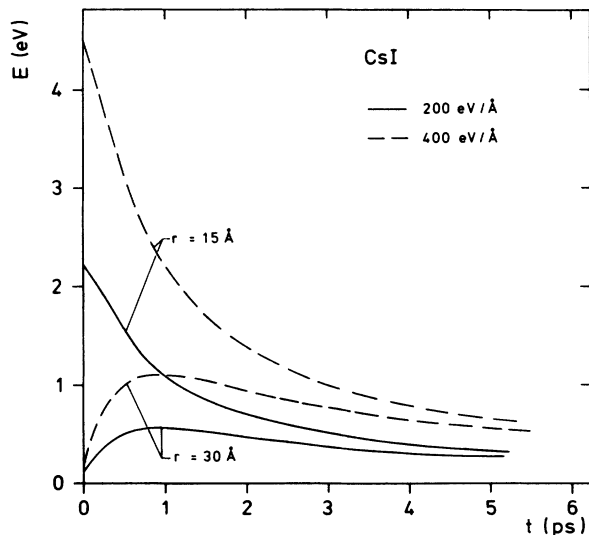


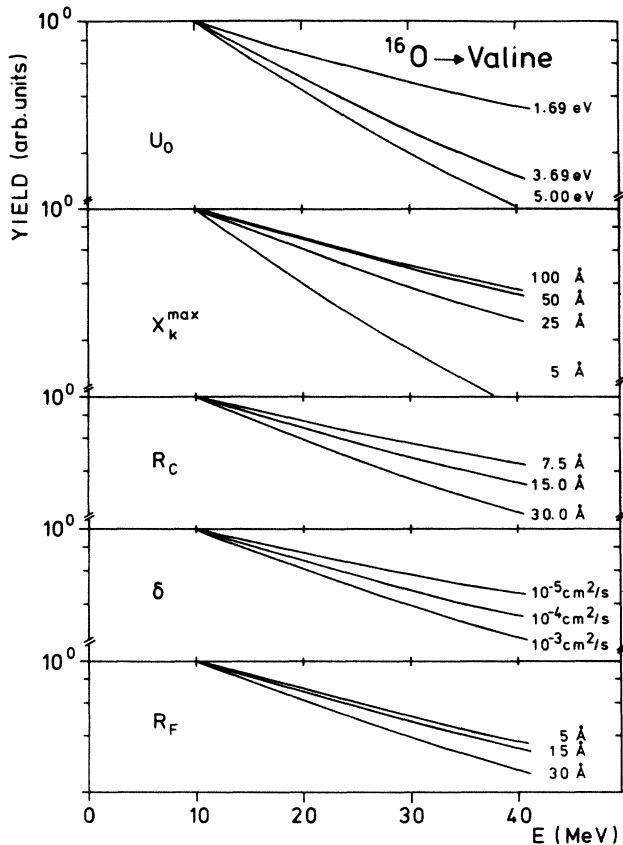FIG. 21. Temporal energy distributions for CsI calculated according to Eq. (3). For details see the caption of Fig. 20.

FIG. 22. Influence of the model parameters on calculated yield functions. The primary ion is $^{16}$O, the sample is valine. Only one parameter (indicated at the left-hand side of the figure) of the standard parameter set was changed each time. The standard parameter set consists of the values given in Table I, $R_C = R_F = 15$ Å and $X^{max} = 50$ Å.

given in Table I together with $R_C = 20$ Å, $R_F = 0$, and $X^{max} = 50$ Å.

## V. COMPARISON BETWEEN CALCULATIONS AND DATA

Model calculations have been performed only for valine and CsI since for all other samples the necessary parameters were not available. Nevertheless characteristic trends in the data of these samples are discussed below in the light of the macroscopic model.

### A. Valine

The model calculations were performed with the parameters of Table I and a constant core radius $R_C = 15$ Å. Only in the case of $^{22}$Ne ions was the core radius increased with increasing ion velocity ($R_C = 15-28$ Å) due to the fact that the velocity changes considerably in the energy range considered and exceeds the electronic orbital velocities by far at the highest measured energies (see Ref. 17). The fragmentation radius $R_F$ was considered to be a free parameter. As expected we find that different
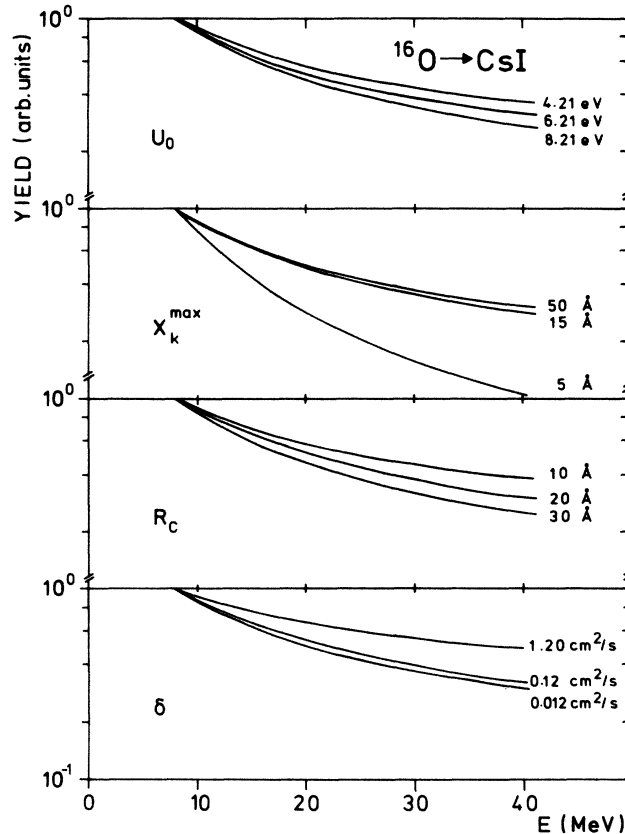
FIG. 23. Influence of the model parameters on calculated yield functions. The primary ion is $^{16}$O, the sample is CsI. The standard parameter set consists of the values given in Table I, $R_C = 20$ Å, $R_F = 0$, and $X^{max} = 50$ Å.

primary ions demand different $R_F$ values due to the different energy losses involved. In the case of $^{16}$O, $^{32}$S, and $^{86}$Kr primary ions the fragmentation radii $R_F$ were taken to be constant over the energy range studied. This is justified since the energy loss change is relatively small. For $^{22}$Ne ions the fragmentation radius $R_F$ was decreased
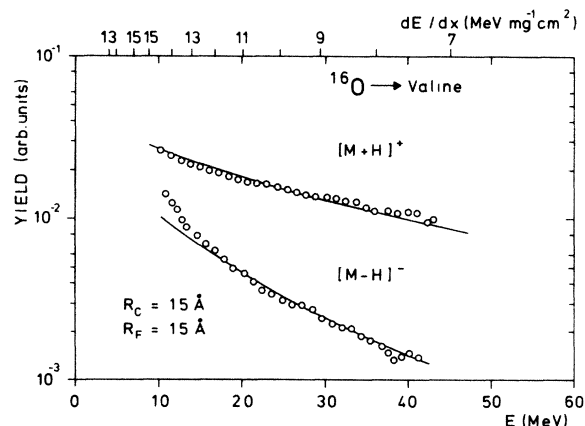


FIG. 24. Comparison between measured yield functions and model calculations (solid lines). The primary ion is $^{16}$O, the sample is valine. The standard parameters of Table I were used for the calculations together with $R_C = R_F = 15$ Å and $X^{max} = 50$ Å.
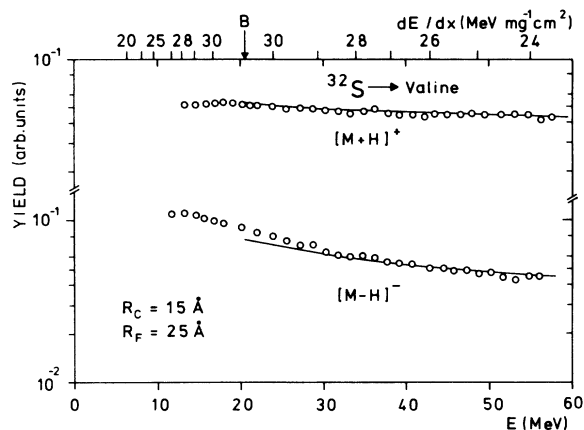
FIG. 25. Comparison between model calculations (solid line) and experimental data. The primary ion is $^{32}$S, the sample is valine. The standard parameters of Table I were used together with $R_C = 15$ Å and $R_F = 25$ Å. $B$ indicates the approximate position of the energy-loss maximum.

with decreasing energy loss (see Fig. 6).

The effective binding energy $U_0$ for $[M-H]^-$ ions was increased by 2 eV compared to the value for $[M+H]^+$ ions in order to simulate the effect of the deprotonation.

Figures 24, 25, 6, and 7 show that reasonable agreement can be obtained between data and calculations. This is also evident from Fig. 8 which shows the $[M+H]^+$ yields for valine obtained with different primary ions as a function of the primary-ion energy loss. The two curves shown in Fig. 8 represent model calculations performed with $R_C = R_F = 15$ Å (solid curve) and $R_C = 15$ Å, $R_F = 40$ Å (dashed curve). It is obvious that an overall agreement can be achieved if the fragmentation radius $R_F$ is increased with increasing projectile mass (i.e., increasing energy loss).

## B. Organic compounds

Yield functions of all other amino acids investigated exhibit energy dependences very similar to those obtained for valine. This is to be expected in the light of the present model since the density and the effective binding energy of valine and other amino acids are comparable[19] and since one can safely assume that the thermophysical properties are also very similar. The fact that the $^{86}$Kr-induced yield for the $(TBA)^+(TPB)^-$ sample increases with decreasing energy loss (see Fig. 13) can be explained with an energy-loss dependent fragmentation radius $R_F$. In fact, in the lower part of Fig. 13 it is shown that the Kr-induced yield increases with increasing energy if a slowly decreasing fragmentation radius (with increasing energy) is used for the calculation (the standard parameter set for valine was adopted). The increase of the yield for the molecular ion due to a decreasing fragmentation radius is related with a decrease of the yield function for fragment ions as observed experimentally (see Fig. 13).

The fact that the $(TPB)^-$ yield functions obtained from

the $^{16}$O, $^{32}$S, and $^{86}$Kr irradiation of the $(TBA)^+(TPB)^-$ sample exhibit a steeper slope than the corresponding $(TBA)^+$ yield functions (see Figs. 10, 12, and 13) cannot be explained with a somewhat larger $U_0$—value for negative ions compared to positive ions as in the case of the valine sample, nor can it be due to the effect of the Coulomb repulsion since $R_F \gg 0$ (see Sec. V C). A possible explanation could be that a larger fragmentation radius exists for the anion compared to the cation due to the larger anion radius. A larger value of $R_F$ leads, however, to a steeper slope (see Fig. 22).

## C. CsI

The model calculations for the CsI sample were performed with the parameters of Table I. The core radius $R_C$ was kept constant for all primary ions ($R_C = 20$ Å). The fragmentation radius $R_F$ was set to zero since it was assumed that secondary ions emerge in this particular case also from the inner region with high-energy density.

Figure 14 shows results of these calculations for $^{16}$O-induced yields (solid lines). The calculations give identical energy dependences for $Cs^+$ and $I^-$ secondary-ion yields as opposed to the experimental result. This is due to the fact that the Coulomb repulsion is not included in the model calculations. Most probably, however, it plays a role for the desorption from a CsI sample. The Coulomb repulsion affects mainly the $Cs^+$ yield since $Cs^+$ ions are desorbed from the hot core region exhibiting a very high positive-charge density localized around the primary-ion track. $Cs^+$ ions are repelled out of this region. The effect becomes the more important the higher the charge density, i.e., the higher the energy loss of the primary ion. It can be simulated in the macroscopic model if one decreases the effective binding energy $U_0$ with decreasing energy. A variation of the $U_0$ value as shown in the inset of Fig. 14 results in the dashed curve which reproduces the data rather well.

The $I^-$ ions apparently are not affected by the Coulomb effect. This means that they do not originate from the hot core region with high charge density. This can be understood if one realizes that only neutral iodine atoms or positively charged ions exist within the hot core region (besides $Cs^+$ ions) due to the fact that the electron affinity and the ionization energy of iodine is small compared to the ionization energy for the $5p$ electrons in cesium. In fact, calculations for the $I^-$ yield performed with $R_F > 0$ give better agreement with the data (the dashed-dotted line in Fig. 14 is calculated with $R_F = 20$ Å). The observation that the absolute yield for $I^-$ ions is always smaller than for $Cs^+$ ions (see Figs. 14 and 16) points into the same direction. The steeper slopes of the yield functions for cluster ions (as compared to that of $I^-$) are also an indication for the existence of a fragmentation region.

The effect of the Coulomb repulsion is also visible in the $^{22}$Ne-induced yield function for $Cs^+$ (see Fig. 15); it does not show up in the $^{32}$S-induced data (the slopes for the $Cs^+$ and $I^-$ yield functions are equal, see Fig. 16) since the energy loss for $^{32}$S is almost constant in the energy range studied.

## VI. SUMMARY

Desorption yield data obtained for different primary ions and different samples could be described consistently in the frame work of a macroscopic model which needs only the thermophysical properties of the sample and the effective binding energy of the surface molecule as input parameters. Coulomb effects which exist for the desorption from a CsI sample can be roughly accounted for. It would be interesting to investigate the dependence of the secondary-ion yield on the primary-ion charges also in the framework of the macroscopic model. This will be the subject of a forthcoming paper.

[1]D. F. Torgerson, R. P. Skrowronski, and R. D. Macfarlane, Biochem. Biophys. Res. Com. **60**, 616 (1974).

[2]See, e.g., J. Mass Spectrom. Ion Phys. **53**, 1 (1983).

[3]B. Nees, E. Nieschler, N. Bischof, P. Dück, H. Fröhlich, W. Tiereth, and H. Voit, Radiat. Eff. **77**, 89 (1983).

[4]B. Nees, E. Nieschler, N. Bischof, H. Fröhlich, K. Riemer, W. Tiereth, and H. Voit, Surf. Sci. **145**, 197 (1984).

[5]R. R. Lucchese, J. Chem. Phys. **86**, 443 (1987).

[6]L. E. Seiberling, J. E. Griffith, and T. A. Tombrello, Radiat. Eff. **52**, 201 (1980).

[7]C. C. Watson and T. A. Tombrello, Radiat. Eff. **89**, 263 (1985).

[8]A. Hedin, P. Håkansson, B. Sundqvist, and R. E. Johnson, Phys. Rev. B **31**, 1780 (1985).

[9]B. V. King, A. R. Ziv, S. H. Lin, and I. S. T. Tsong, J. Chem. Phys. **82**, 3641 (1985).

[10]P. Dück, H. Fröhlich, W. Treu, and H. Voit, Nucl. Instrum. Methods **189**, 615 (1981).

[11]P. Dück, W. Treu, H. Fröhlich, W. Galster, and H. Voit, Surf. Sci. **95**, 603 (1980).

[12]H. J. Bestmann, Angew. Chem. **89**, 361 (1977).

[13]C. J. McNeal, R. D. Macfarlane, and E. L. Thurston, Anal. Chem. **51**, 2036 (1979).

[14]L. C. Northcliffe and R. F. Schilling, Nucl. Data Tables A7, 233 (1970).

[15]J. F. Ziegler, *Handbook of Stopping Cross Sections for Energetic Ions in All Elements* (Pergamon, New York, 1980).

[16]P. Dück, Ph.D. thesis, University of Erlangen-Nürnberg, 1980 (unpublished).

[17]A. Mozumder, Adv. Radiat. Chem. **1**, 1 (1969).

[18]N. Bohr, Philos. Mag. **25**, 10 (1913).

[19]H. J. Svec and D. D. Clyde, J. Chem. Eng. Data **10**, 151 (1965).

[20]J. O. Hutchens, A. G. Cole, and J. W. Stout, J. Phys. Chem. **67**, 1128 (1963).

[21]*American Institute of Physics Handbook*, 2nd ed., edited by Dwight E. Gray (McGraw-Hill, New York, 1963).

[22]G. H. Aylward and T. J. V. Findlay, *Datensammlung Chemie in SI-Einheiten* (Verlag Chemie, Weinheim, 1981).

[23]F. Reif, *Fundamentals of Statistical and Thermal Physics* (McGraw-Hill, New York, 1965).

[24]*Thermophysical Properties of Matter, The TPRC Data Series*, edited by Y. S. Touloukian (IFI/Plenum, New York, 1970).